PHYSICAL SCIENCES

Femtosecond visualization of oxygen vacancies in metal oxides

Xinping Zhang[1]*, Fawei Tang[2], Meng Wang[1], Wangbin Zhan[2], Huaxin Hu[2], Yurong Li[2], Richard H. Friend[3]*, Xiaoyan Song[2]*

Oxygen vacancies often determine the electronic structure of metal oxides, but existing techniques cannot distinguish the oxygen-vacancy sites in the crystal structure. We report here that time-resolved optical spectroscopy can solve this challenge and determine the spatial locations of oxygen vacancies. Using tungsten oxides as examples, we identified the true oxygen-vacancy sites in $WO_{2.9}$ and $WO_{2.72}$, typical derivatives of WO_3 and determined their fingerprint optoelectronic features. We find that a metastable band with a three-stage evolution dynamics of the excited states is present in $WO_{2.9}$ but is absent in $WO_{2.72}$. By comparison with model bandstructure calculations, this enables determination of the most closely neighbored oxygen-vacancy pairs in the crystal structure of $WO_{2.72}$, for which two oxygen vacancies are ortho-positioned to a single W atom as a sole configuration among all O—W bonds. These findings verify the existence of preference rules of oxygen vacancies in metal oxides.

INTRODUCTION

As important and extensively interested forms of condensed matter, metal oxides have been within the focused investigations in many disciplinary fields, which include various dielectric (*1*, *2*), semiconductor (*3*–*5*), and conductive materials (*6*, *7*). Multivalency is one of the most notable aspects of metal oxides owing to the varying degrees of oxygen deficiency. Accordingly, metal oxides with various valence states may have distinctly different characteristics, which define their individual applications. Typically, oxidation products of tungsten with decreasing oxygen concentrations, e.g., WO_3, $WO_{2.9}$, and $WO_{2.72}$, are typical derivatives with different stoichiometric ratios (*8*, *9*). Although electrochemical methods have been used to control the oxygen content in metal oxides (*8*, *10*, *11*) and doping tungsten thin films with oxygen was demonstrated for spintronic investigations (*12*), $WO_{2.9}$ and $WO_{2.72}$ are generally representative products of stepwise reduction reactions of WO_3 through "removal" of oxygen from the lattices (*13*, *14*), producing oxygen vacancies. These oxygen deficiencies are well known to have a large effect on electronic properties. WO_3 is a wide-gap semiconductor; however, as oxygen vacancies are introduced, the Fermi energy is moved into the tungsten-based conduction band, and $WO_{2.9}$ and $WO_{2.72}$ exhibit metallic characteristics. Owing to these features, in addition to their commonly interested applications in ceramic capacitors, photochromic devices, solar cells, and coloring agents, $WO_{2.9}$ is more suitably applied in smart glass and photosensitive sensors, whereas $WO_{2.72}$ is more widely used in gas sensors in the detection of reductive or oxidative molecules (*15*–*17*). These groups of gas sensors are based on the electronic exchange between the detection target and the metal oxide at their interface during the reduction/oxidization processes, where oxygen vacancies play crucial roles in realizing the chemiresistive response. When tungsten oxides are used as sensing materials for gas molecules of NO_2, SO_2, NH_3, etc., the oxygen vacancies give n-type semiconductor behavior that controls the sensing mechanisms (*18*). Therefore, precise determination and control of oxygen content in these metal oxides are of key importance.

On the basis of these considerations, revealing the structural evolution due to the change in oxygen content is of great significance for further investigations and applications of metal oxides. The scientific question that we address here is whether the oxygen vacancies have specific preference in their locations, so that there are defined lattice configurations for the electrovalence-changeable oxides. Conventionally, microscopic characterization with high resolution is required to examine the defects in crystal structures. To date, even the most advanced microscopic techniques have not been able to resolve the oxygen vacancies produced during the transformations between derivatives of metal oxides. Although the color appearance may supply some identifications, the corresponding broadband steady-state spectroscopic response cannot justify the oxygen-vacancy characteristics. However, oxygen vacancies influence the key photoelectronic performance through modifying the bandstructures, where transitions between the fine electronic states in metals, metal oxides, and semiconductors are generally in time scales ranging from femtoseconds to picoseconds (*19*–*21*). Ultrafast spectroscopy is thus an effective approach for resolving precisely the collective electronic behaviors in metals (*22*, *23*), inter-/intraband transitions and energy-level distributions in semiconductors (*24*, *25*), nonlinear optical and electronic behaviors in ferromagnetic alloys (*26*, *27*), and spintronic performance in metal oxides (*28*, *29*).

We use here ultrafast spectroscopy as a precise approach to clarifying the fine modifications by oxygen vacancies on photoelectronic performance of metal oxides, thus identifying how the oxygen vacancies are arranged in the crystal structures in terms of their numbers and locations. Using tungsten oxides as examples, we have not only found the true configurations of oxygen vacancies in the derivatives of WO_3 but also determined their bandstructures with precisely evaluated lifetimes and photoelectronic transitions. These scientific findings are based on the alignment between bandstructures resolved by the distribution of total density of states (TDOS) and electronic transitions revealed by the femtosecond multiphoton transient absorption (TA) spectroscopy (*30*, *31*), which is, in nature, a femtosecond visualization (fsV) of the oxygen-vacancy

[1]Institute of Information Photonics Technology and College of Applied Sciences, Beijing University of Technology, Beijing 100124, China. [2]College of Materials Science and Engineering, Key Laboratory of Advanced Functional Materials, Education Ministry of China, Beijing University of Technology, Beijing 100124, China. [3]Cavendish Laboratory, University of Cambridge, Cambridge CB3 0HE, UK.
*Corresponding author. Email: zhangxinping@bjut.edu.cn (X.Z.); rhf10@cam.ac.uk (R.H.F.); xysong@bjut.edu.cn (X.S.)

configurations. The microscopic challenge is thus solved by time-resolved spectroscopy.

RESULTS AND DISCUSSIONS

Crystal structure models for fsV of oxygen-vacancy configurations in metal oxides

The basic principle of fsV is illustrated schematically in Fig. 1. Oxygen vacancies (O-V) induce defect states in the electronic bandstructures of metal oxides, the correspondence between which is highlighted by dashed circles. These modifications lead to unique photoelectronic transitions under optical excitation. This gives optical spectroscopy an opportunity to probe these bandstructure modulations by projecting the "fingerprint" pictures in terms of TA as a function of photon energy ($h\nu$) and the time delay (τ) between the femtosecond pump and probe pulses. However, there are multiple possibilities in the configuration of the oxygen vacancies in terms of their numbers and locations for each metal oxide. Fortunately, the first-principle modeling on the crystal structures may supply basic evaluation on the electronic bands by TDOS. Thus, alignment of the TDOS distribution with the femtosecond TA spectroscopic response enables sole determination of the true configuration, corresponding to the perfect TDOS-TA matching. "Alignment" here can be understood as the direct correspondence between the energy levels determined by multiphoton ultrafast spectroscopy and the calculated bandstructures as TDOS spectra, which are scaled with a same energy axis. The meaning of alignment will be more clearly demonstrated by the analysis of the experimental results in the following sections.

As for tungsten oxides, it can be inferred from the Gibbs free energies (fig. S1) (*32*), WO_3 is thermodynamically the most stable, and it has a monoclinic crystal structure (*33*, *34*); meanwhile, $WO_{2.9}$ exhibits much higher thermodynamic stability than $WO_{2.72}$. Compared with WO_3, $WO_{2.9}$ and $WO_{2.72}$ have roughly 3.33 and 9.33% oxygen deficiencies, respectively. Thus, the local atomic configurations of $WO_{2.9}$ and $WO_{2.72}$ can be modeled by removing one and two oxygen atoms, respectively, from the unit cell of WO_3, as shown in Fig. 2. To model the atomic configuration of $WO_{2.9}$, an oxygen atom at the position marked by the red circle in Fig. 2B is removed from the crystal structure of WO_3 shown in Fig. 2A. Considering the symmetry of the crystal structure, the position of this oxygen vacancy is not critical for $WO_{2.9}$, as can be verified through first-principle calculations (fig. S2). However, in modeling $WO_{2.72}$, two oxygen atoms must be removed from two different locations. Hence, there exist multiple combinations of such oxygen-vacancy pairs. Again, on the basis of the symmetry of the crystal structure, four possible configurations exist, as shown in Fig. 2C by labels ①, ②, ③, and ④. The red circles in Fig. 2C indicate the positions of the two oxygen vacancies.

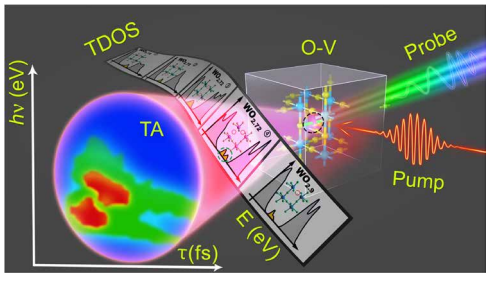

Fig. 1. Schematic illustration of the fsV principles. Femtosecond laser pulses (pump) excite the oxygen vacancy (O-V)–contained metal oxides. Interaction of broadband supercontinuum pulses (probe) with the excited states characteristic of the oxygen vacancies induces a spectroscopic picture of TA as a function of photon energy ($h\nu$) and time delay (τ). Alignment of TA ($h\nu$, τ) with the distribution of the TDOS with photon energy E enables precise determination of the unique oxygen-vacancy arrangement for a given metal oxide. The slides present schematically the varied chemical structures and TDOS spectra for different O-V configurations of $WO_{2.9}$ and $WO_{2.72}$. The black dashed circle highlights a schematic O-V site. The dashed green ring on one of the slides highlights the defect state plotted as TDOS spectrum calculated on a specific O-V structure in $WO_{2.72}$. The correlation between the tentative O-V structures, the TDOS spectra, and the measured TA dynamics enables determination of the true O-V configuration through precise matching between the TDOS and TA performance.

Figure 2 (D and E) presents first-principle calculations of the TDOS distribution, corresponding to the models in Fig. 2 (A to C). Because the bandgap of WO_3 is larger than 3.0 eV, an exciting photon at 3.1 eV or two-photon excitation (2PE) at 1.55 eV can only induce weak transitions between the band edges and subsequent exciton absorption of the probe pulses. This is confirmed by the measurements shown in fig. S3. However, removing an oxygen atom induces defect states in $WO_{2.9}$ within the intrinsic bandgap of WO_3, as indicated by the red ovals in Fig. 2D. Consequently, the bandgap is reduced to 0.54 eV for $WO_{2.9}$, and the Fermi level passes through the defect band. In addition, the whole bandstructure intrinsic to WO_3 is lowered by about 3.0 eV with respect to the Fermi level. These modifications lead to completely different electronic transitions under optical excitation, enabling definition of femtosecond fingerprint features of $WO_{2.9}$.

In Fig. 2E, the black curves show the TDOS of $WO_{2.72}$ calculated for the four configurations of oxygen vacancies labeled ①, ②, ③, and ④ in Fig. 2C. For comparison, the TDOS of $WO_{2.9}$ is also shown as the red curve in each plot in Fig. 2E. Comparing $WO_{2.72}$ with $WO_{2.9}$ for configurations ①, ②, and ③, we observe negligible changes in the bandstructures, in particular, for the bandgaps indicated by the downward red triangles at roughly 0.5 and 2.5 eV. However, substantial differences are observed in configuration ④: (i) the bandgap centered at 2.5 eV is smeared by a notable increase in TDOS and by the red shift of the band edge; (ii) the bandgap at about 0.5 eV has a much reduced modulation depth in the TDOS spectrum owing to the overlap between the two adjacent bands; (iii) in contrast to configurations ①, ②, and ③, the state peaked at about −0.8 eV (blue triangle) is much stronger than that with the Fermi level ($E = 0$) passing through. These three features are highlighted in yellow in the plot of configuration ④. However, according to calculations of the formation energies (*13*) listed in table S1, the differences between configurations ① and ④ are extremely small, although configuration ③ has the lowest value and ④ has the highest, suggesting ③ as the most probable structure and ④ as the improbable structure. All these factors present big challenges in determining the true crystal structure regarding oxygen-vacancy sites from the configurations shown in Fig. 2. Furthermore, the crystal structure modeling in Fig. 2 shows weak bandstructure modulation, which induces fine deviations of the photoelectronic transitions between different models. Therefore, optical spectroscopic investigation with high temporal and spectral resolution is required to disclose the involved photoelectronic processes. This motivates the employment of femtosecond pump-probe spectroscopy to determine the true bandstructures and accomplish the oxygen-vacancy visualization.

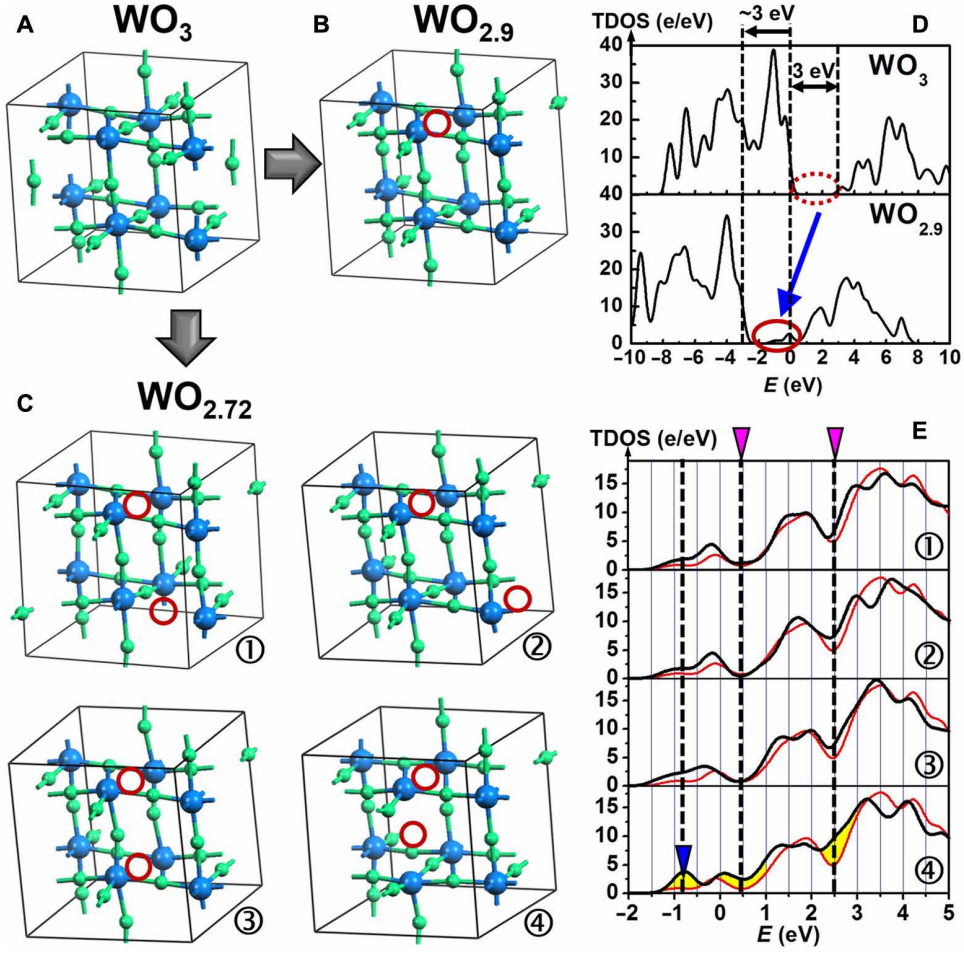

Fig. 2. Crystal structure models and TDOS calculation results. Local structural configurations of (**A**) WO_3, (**B**) $WO_{2.9}$, (**C**) $WO_{2.72}$ and the corresponding TDOS distributions for (**D**) WO_3 (top)/$WO_{2.9}$ (bottom) and (**E**) $WO_{2.72}$ (①, ②, ③, and ④).

fsV of oxygen-vacancy configuration in $WO_{2.9}$

Figure 3A shows a three-dimensional (3D) picture of the reflective TA spectroscopic measurements on $WO_{2.9}$ for a probe photon of 1.4 to 1.95 eV and a time delay of 0 to 1 ps when pumped at 1.55 eV. We used a pump fluence of 400 μJ/cm^2 for all measurements, unless otherwise specified. The white curve labeled "ΔA = 0" in Fig. 3A is the interface between positive and negative TA signals. The area enclosed by the white curve corresponds to positive TA with $0 < \Delta A < 15$ mOD ($10^{-3}\times$ optical density).

The most notable feature in Fig. 3A is the strong negative TA within the first 380 fs identified by the black "deep hole" highlighted by a triangle, which is centered around 1.61 eV as indicated by the leftward magenta arrow. This deep hole is also indicated by a downward triangle in the inset of Fig. 3B for the blue curve. The TA dynamics reverts to positive after 400 fs, which is shown more clearly in fig. S4 (A and B). For the TA dynamics at 1.61 eV in Fig. 3B, an oscillation occurs, and the signal reverts to negative after 2 ps and then stays there. The TA dynamics for a time delay as long as 900 ps at 1.50, 1.52, and 2.22 eV are included for comparison in Fig. 3B and those within the first 2 ps in the inset. The TA signal is definitely positive at 1.50 and 1.52 eV, whereas it is negative at 2.22 eV over the whole dynamics, agreeing well with Fig. 3A.

In addition to the oscillation dynamics at 1.61 eV, all TA dynamic curves comprise multiple stages. A typical measurement at 1.52 eV is shown in Fig. 3C. Considering the pulse length of 150 fs, the fast process with a lifetime $\tau_1 \approx 310$ fs, according to the fit, is clearly a two-photon absorption (2PA) process, wherein one pump and one probe photons are absorbed, as also observed in organic semiconductors (*35*, *36*). The slowest process, with a lifetime $\tau_3 > 1$ ns, according to the measurement shown in Fig. 3B and the fit in Fig. 3C, is attributed to absorption by excitons on the lower edge of the excitation band. Between the fast and slowest processes, there exists an intermediate process with a lifetime $\tau_2 < 3$ ps. This intermediate stage can also be observed in the TA dynamics when pumping at 3.1 eV with a fluence of 100 μJ/cm^2, as shown in fig. S5, which results in three-stage evolution dynamics. Both dynamic curves measured at 1.61 and 1.52 eV for pumping at 3.1 eV exhibit three stages, as guided by the dashed lines. The measurement results in Fig. 3C and fig. S5 provide evidence for the existence of a metastable excited state, which is designated as E_n, above the lowest exciton state E_m, as depicted in the inset of Fig. 3C and in Fig. 3D, which is responsible for the intermediate TA stage with $\tau_2 < 3$ ps.

Both the oscillation (at 1.61 eV) and the three-stage features in the TA dynamics originate from the same photoelectronic mechanism.

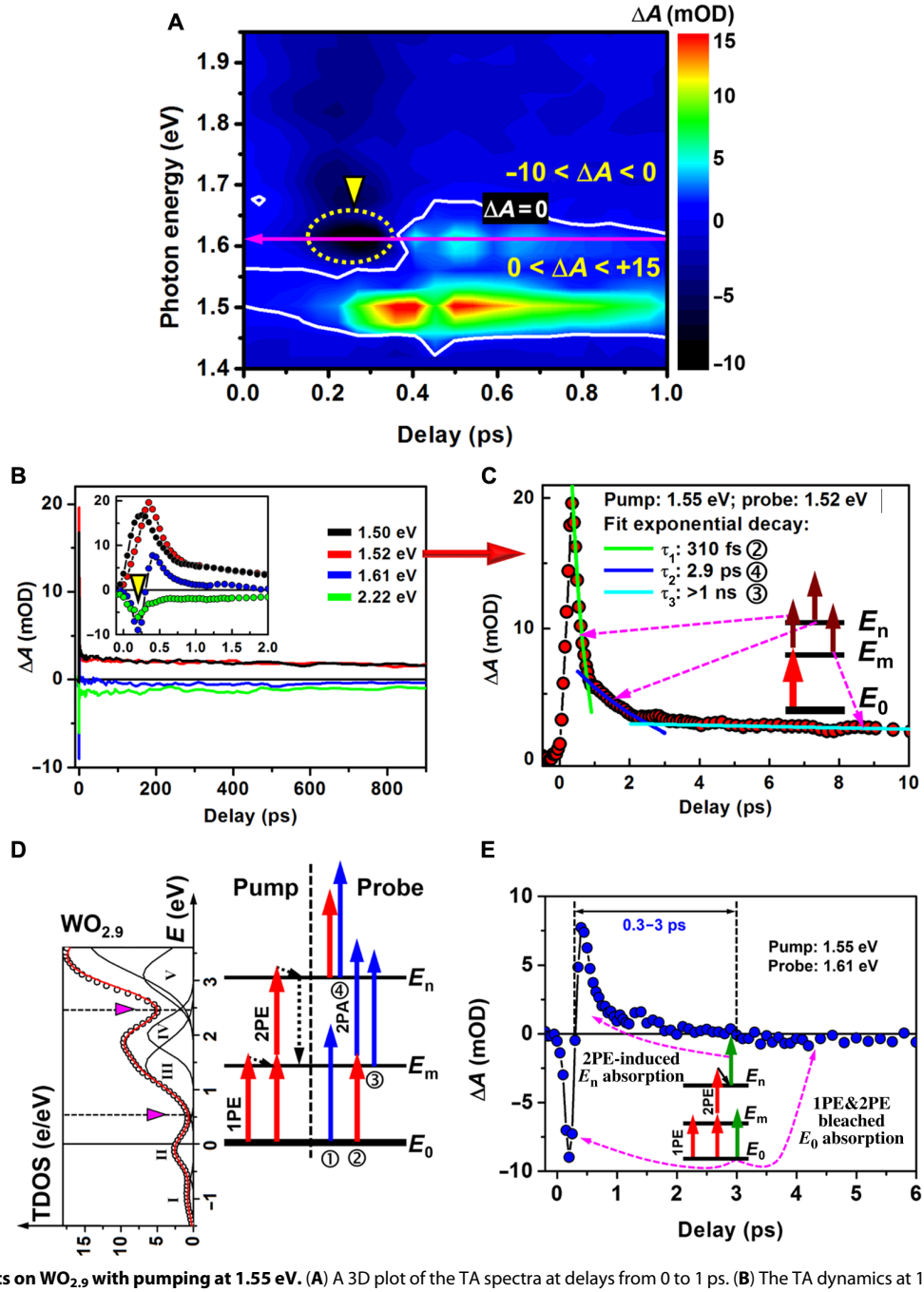

Fig. 3. TA measurements on $WO_{2.9}$ with pumping at 1.55 eV. (**A**) A 3D plot of the TA spectra at delays from 0 to 1 ps. (**B**) The TA dynamics at 1.50, 1.52, 1.61, and 2.22 eV for a time delay from 0 to 900 ps. Inset: An expanded view of the delay range of 0 to 2 ps. (**C**) TA dynamics at 1.52 eV used to determine the lifetimes of the involved transition processes. Inset: Related photoelectronic transitions. (**D**) Alignment of the calculated TDOS with the transitions resolved from the measured TA spectra. (**E**) Detailed analysis of the oscillatory TA dynamics at 1.61 eV. Inset: 2PA- and 2PE-enhanced E_n absorption, bleached E_0 absorption.

For better understanding, we aligned the calculated TDOS for $WO_{2.9}$ with the electronic transitions revealed by the TA spectra, as shown in the left panel of Fig. 3D. The open circles in the left panel of Fig. 3D show the calculated TDOS distribution, and the solid red curve is a fit using multiple Gaussian functions, which are represented by the solid black curves and defined as bands I to V. There is little overlap between bands II and III and between bands IV and V, leaving two gaps indicated by magenta triangles. The defect states correspond to bands I and II, and the Fermi level with $E = 0$ goes through band II. The lowest excited state is located at the lower edge of band III. It is defined as E_m and has a lifetime of >1 ns, where the excitons relax by transition back to E_0. The higher-lying excited state, which has a lifetime shorter than 3 ps, is defined as the metastable state E_n and is included in band V. These energy levels, together with the possible electronic transitions involved in the pump-probe process, are depicted in the right panel of Fig. 3D. Single-photon excitation (1PE) at 1.55 eV

produces exciton population at E_m, with a lifetime τ_3, and 2PE induces a population at E_n with a lifetime τ_2. Thus, the TA process involves ① bleaching of the ground-state absorption at E_0, ② 2PA through absorbing one pump and one probe photon by the ground-state molecules, ③ absorption by excitons at E_m, and ④ absorption by excitons at E_n. The bleaching process ① is responsible for the negative TA spectrum with photon energies larger than 1.55 eV. Therefore, the three stages of the positive TA dynamics shown in Fig. 3C correspond exactly to the processes ②, ③, and ④. On the basis of the inset in Fig. 3B, the dynamics at 1.52 eV has a relatively slow rise. This is understood as some remaining bleaching of the ground-state absorption at 1.52 eV, implying that E_m is located just between 1.50 and 1.52 eV. Moreover, the 2PA process ② stopped suddenly at 1.44 eV, implying that E_n is located at 1.55 + 1.44 = 2.99 eV. Thus, we can align E_m and E_n with the TDOS peaks of bands III and V, respectively. Furthermore, we can relate the three stages of TA dynamics in Fig. 3C and fig. S5 directly to the photoelectronic transitions, as shown in the insets with dotted arrows indicating the correspondence.

Figure 3E explains how E_n is responsible for the oscillatory feature in the TA dynamics at 1.61 eV, where transition from E_0 to E_m is definitely allowed for excitation at 1.61 eV. Bleaching of the ground-state absorption dominates the TA dynamics at the arrival of the pump pulses, where 1PE and 2PE pump the E_0 molecules to populate E_m and E_n, respectively. Thus, negative TA is observed in the first 300 fs in Fig. 3E. Simultaneously, the 2PA process in which one pump and one probe photon are absorbed is modulated by two opposing processes: enhancement due to the temporal pump-probe overlap and the 2PE bleaching of the absorption at E_0. However, we focus our discussions mainly in the delay range from 0.3 to 3 ps, where there is nearly no overlap between the pump and probe pulses after 300 fs, considering a pulse length of about 150 fs. Therefore, we did not include the 2PA process in the energy-level diagram in Fig. 3E, which can be basically ruled out for the positive TA–dominated dynamics from 300 fs to 3 ps. Notably, with increasing the population on E_n due to 2PE, the exciton absorption at E_n becomes substantial. Owing to the shorter lifetime of E_n than 3 ps, the TA by the E_n excitons can be observed in the early stage of the dynamics, when it survives other competitive bleaching processes and induces the turn from falling to rising dynamics at 200 fs, with subsequently positive TA dynamics at 300 fs. Thus, the positive TA "peak" in Fig. 3E is definitely attributed to absorption by E_n excitons, as highlighted by the dashed arrow labeled with "2PE-induced E_n absorption." After the E_n absorption, the long-lived bleaching process dominates the TA dynamics again, such that the TA becomes negative after 3 ps. The energy-level diagram in Fig. 3E summarizes these electronic transitions, and the dashed arrows relate them to their respective TA dynamics. The dynamics from 0.3 to 3 ps agrees well with E_n absorption in the second stage of TA in Fig. 3C and fig. S5, indicating consistent evidence.

The excitonic behavior on E_n can be more clearly distinguished from other TA dynamics by the pump fluence dependence. In fig. S6 (A and B), we present the TA dynamics at 1.61 and 1.50 eV, respectively, for pumping at 1.55 eV with the pump fluence increased from 100 to 500 μJ/cm^2. 2PE induced exciton population on E_n, resulting in a quadratic dependence of the bleaching of ground-state TA on the pump fluence, as shown in fig. S6C. This mechanism is responsible for the negative TA in the first stage of the oscillatory dynamics at 1.61 eV. Meanwhile, because of the existence of the metastable state of E_n, the corresponding exciton absorption should increase with a quadratic dependence on the pump fluence. However, the pump pulse also excites the E_n excitons, bleaching the E_n absorption. These two opposite processes worked together on the interaction between the probe and the E_n excitons, resulting in a first increase, followed by a decrease variation in the pump fluence dependence, as shown in fig. S6 (B and D). Descriptions are also included in the Supplementary Materials.

fsV of oxygen-vacancy configurations in $WO_{2.72}$

Figure 4A shows a 3D picture of the TA signal for probe photon energies of 1.4 to 1.95 eV and for delay times of 0 to 1 ps. Large differences can be observed between Fig. 4A and Fig. 3A in the following features: (i) the oscillatory dynamics at 1.61 eV is not observed in Fig. 4A, instead, the TA signal remains positive over the whole dynamics. (ii) The positive TA extends from 1.42 to as much as 1.90 eV, as shown by the white curve that defines the boundary of ΔA = 0 in Fig. 4A, which is much broader than that for $WO_{2.9}$. This is more clearly shown in fig. S7 by comparing the TA spectrum for $WO_{2.72}$ at a delay of 0.4 ps and those for $WO_{2.9}$ at delays of 0.25 and 0.4 ps. Comparison showed that the positive band of the $WO_{2.72}$ TA spectrum is more than 0.3 eV broader. (iii) The amplitude of the TA signal for $WO_{2.72}$ is enhanced by a factor of more than 5 (80/15 = 5.33) with respect to $WO_{2.9}$, as also shown in fig. S7.

The most important fingerprint of $WO_{2.9}$ is the existence of the higher-lying metastable excited state E_n, as shown in Figs. 2C and 3A. However, it disappears for $WO_{2.72}$, as shown in Fig. 4B. In Fig. 4B, we plotted the TA dynamics at 1.60 and 1.51 eV for pumping at 1.55 eV (yellow- and blue-filled circles, respectively) for a delay time range of 0 to 10 ps. The TA dynamics at 1.52 eV for $WO_{2.9}$ is included for comparison and plotted by the empty circles. Only the fast 2PA and the long-lived slow exciton absorption processes are observed for $WO_{2.72}$. The metastable state E_n and the corresponding higher-lying bandgap in $WO_{2.9}$ do not exist in $WO_{2.72}$. Furthermore, even the slow process lives much shorter for $WO_{2.72}$ than for $WO_{2.9}$, as shown in the inset of Fig. 4B, where the TA dynamics is plotted in a delay time range of 20 to 1000 ps. The exciton lifetime is about 500 ps for $WO_{2.72}$ and longer than 1 ns for $WO_{2.9}$.

For understanding the long-term TA dynamics, in addition to the transitions back to the ground states, we need to consider the metallic performance of $WO_{2.9}$ and $WO_{2.72}$ due to introduction of the oxygen-vacancy defects, where the Fermi level goes through the defect states. Bulk plasmon electronic processes have been inevitably induced under optical excitation (*25*). Thus, in addition to the contribution from excitonic absorption, relaxation of the plasmonic electrons that led to energy transfer from the hot electrons to the lattices through electron-phonon and, eventually, phonon-phonon interactions is also responsible for the long-term TA dynamics. Such phonon scattering–based thermal processes last much longer than the electron- and exciton-involved processes, which are generally longer than 500 ps (*37*). This explains the much longer lifetime of $WO_{2.9}$ and $WO_{2.72}$ than the generally expected for metallic materials. Furthermore, interband excitation by femtosecond laser pulses also produced a large amount of conduction band electrons, which are not only involved in the processes of electronic band transitions but also modulate the dynamics of plasmonic electrons (*13*). The above mechanisms are overlapped with the exciton decay dynamics and are together responsible for the observed long tails of the TA dynamics for $WO_{2.9}$ and $WO_{2.72}$.

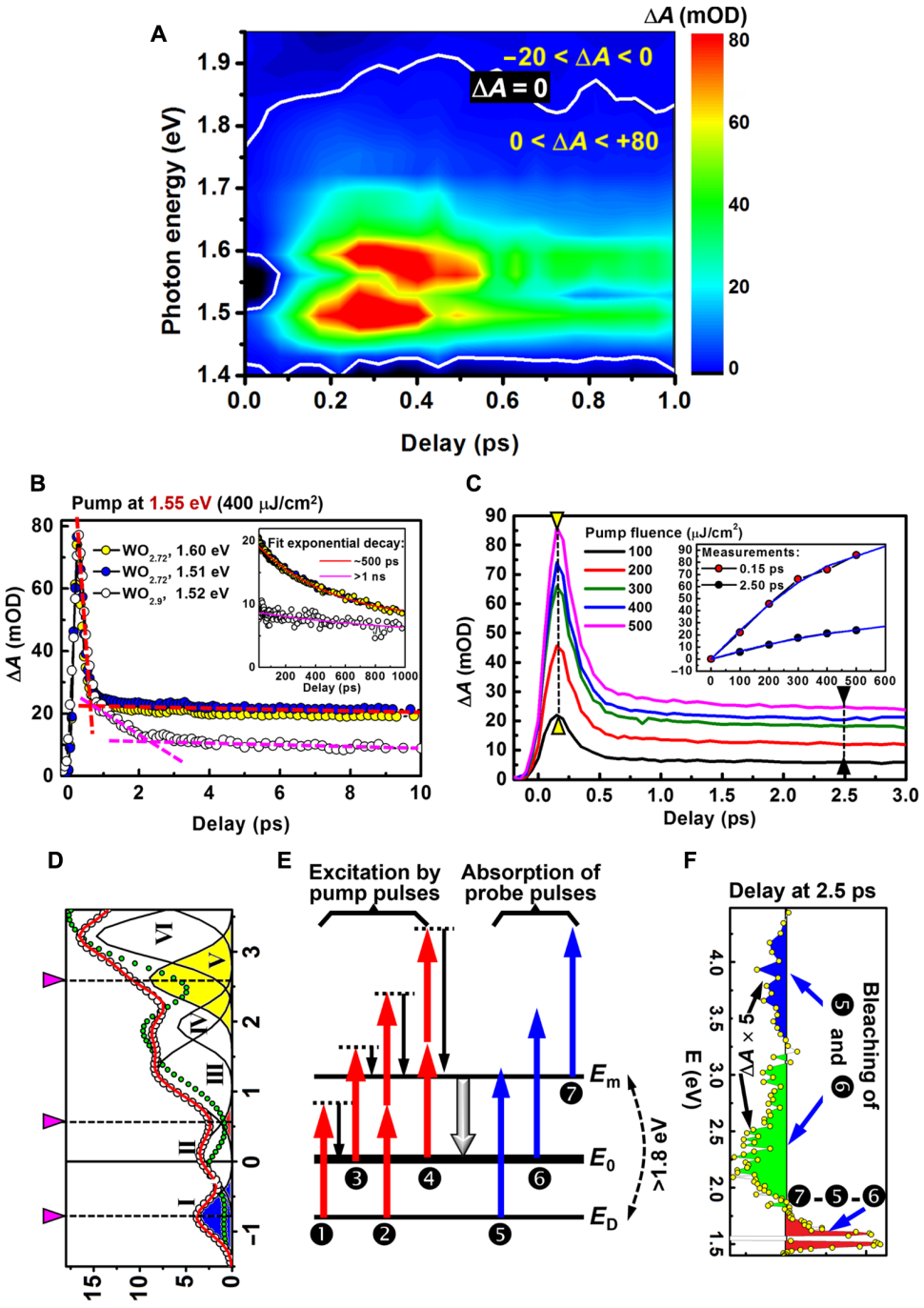

Fig. 4. TA spectroscopic measurements on $WO_{2.72}$ with pumping at 1.55 eV. (**A**) TA as a function of time delay and probe photon energy. (**B**) TA dynamics measured for $WO_{2.72}$ at 1.51 and 1.60 eV and $WO_{2.9}$ at 1.52 eV for a delay time range of 0 to 10 ps, using a pump fluence of 400 μJ/cm^2. Inset: TA dynamics in a delay time range of 20 to 1000 ps. (**C**) Pump fluence dependence of the TA dynamics at 1.60 eV. Inset: Plots of the measured TA amplitude at a delay of 0.15 ps (red circles) and 2.5 ps (black circles) as a function of the pump fluence, together with fits to third-order ($Y = A_1X - B_1X^2 - C_1X^3$) and second-order ($Y = A_2X - B_2X^2$) polynomials, respectively, with $A_1 = 1.23$, $B_1 = 1.65 \times 10^{-3}$, $C_1 = 2 \times 10^{-5}$, $A_2 = 0.35$, and $B_2 = 1.08 \times 10^{-3}$. (**D**) Calculated TDOS for $WO_{2.72}$ (open black circles) and the fit (red solid curve) obtained by decomposing the band distribution into multiple subbands (I to VI, black solid curves). The TDOS for $WO_{2.9}$ (green-filled circles) is included for comparison. (**E**) Proposed energy levels aligned with (D) and possible electronic transitions through excitation by the pump pulses and absorption of the probe pulses. (**F**) The TA spectrum at a delay of 2.5 ps between the pump and probe pulses, resolving the two energy bands I and II that include E_0 and E_D, respectively.

Similar effects can be observed for the TA dynamics when pumping at 3.1 eV, as shown in fig. S8, where the measurements are plotted for a delay time range of 0 to 10 ps. Comparing the TA dynamics at 1.61 and 1.50 eV for $WO_{2.72}$ with that at 1.50 eV for $WO_{2.9}$ in the left panel, we find that the intermediate stage resulting from the metastable state E_n in $WO_{2.9}$ is definitely absent in $WO_{2.72}$.

Furthermore, it is clearly seen that the lifetime of the slow TA process for $WO_{2.72}$ is much shorter than for $WO_{2.9}$, as shown in the inset of fig. S8, where the TA dynamics is plotted for a delay range of 20 to 1000 ps.

These large differences between $WO_{2.72}$ and $WO_{2.9}$ enable us to establish that the true configuration of the oxygen vacancies in $WO_{2.72}$ is that in model ④ in Fig. 2C. Apparently, configurations ① to ③ cannot be assigned to $WO_{2.72}$, because their bandstructures are nearly the same as that of $WO_{2.9}$. Thus, the TA behavior shown in Fig. 4 actually defines the femtosecond fingerprint features of the oxygen vacancies in $WO_{2.72}$. However, such a determination cannot agree with the lowest formation energy rule according to the data in table S1, ruling out the configuration ④. Therefore, for practical metal oxides, the lowest formation energy rule is not reliably applicable for determining the crystal structures, which is based on an average evaluation on the whole system. It needs to be considered that oxygen atoms are lost from local sites to form vacancies.

The pump fluence dependence of the TA dynamics can decompose the mechanisms into more specific details. Figure 4C plots the TA dynamic curves at 1.60 eV when pumped at 1.55 eV, as the pump fluence was varied from 100 to 500 $\mu J/cm^2$. At a delay of 150 fs, the TA dynamics corresponds to 2PA, wherein one pump and one probe photon are absorbed at E_D and E_0, as indicated by the yellow triangles in Fig. 4C and can be described by

$$\Delta A \propto (\sigma_2 N_1 + \sigma_{2D} N_D) I_P I_d \quad (1)$$

where σ_{2D} and σ_2 are the 2PA cross sections at E_D and E_0, respectively; N_1 and N_D are the densities of states at E_0 and at E_D, respectively; and I_P and I_d denote the intensities of the pump and probe pulses, respectively. However, the pump pulses have bleached the ground-state absorption by 1PE and 2PE from E_0 to E_m and from E_D to E_0; thus, we have

$$\Delta A \propto A_1 I_P I_d - B_1 I_P^2 I_d - C_1 I_P^3 I_d \quad (2)$$

with $A_1 = \sigma_2 N_0 + \sigma_{2D} N_{D0}$, $B_1 = (\sigma_2\sigma_1 N_0\tau_P + \sigma_{2D}\sigma_D N_{D0}\tau_P - \sigma_2\sigma_D N_{D0}\tau_P)/h\nu_P$, and $C_1 = (\sigma_2^2 N_0 + \sigma_{2D}^2 N_{D0})\tau_P/2h\nu_P$. Fit to the measured data shown by the red-filled circles in the inset of Fig. 4C agrees very well with the disclosed mechanisms.

For a delay of 2.5 ps, the TA signal results mainly from the absorption by the E_m excitons with a density of N_m and an absorption cross section of σ_m, in combination with bleaching of the ground-state absorption at E_0 and E_D. The population on E_m results from 1PE from E_0 and 2PE from both E_0 and E_D. Note that process ❶ also enhances the population on E_m indirectly through further excitation by ❸. These processes also bleached ground-state absorption. Thus, we have

$$\Delta A \propto \sigma_m N_m I_d - [\sigma_1(N_0 - N_1) + \sigma_D(N_{D0} - N_D)]I_d = A_2 I_P I_d - B_2 I_P^2 I_d \quad (3)$$

with $A_2 = [(\sigma_m\sigma_1 N_0 + \sigma_D\sigma_1 N_{D0}) - (\sigma_1^2 N_0 + \sigma_D^2 N_{D0})]\tau_P/h\nu_P$ and $B_2 = [(\sigma_m\sigma_2 N_0 + \sigma_m\sigma_{2D} N_{D0}) - (\sigma_1\sigma_2 N_0 + \sigma_D\sigma_{2D} N_{D0})]_P/2h\nu_P$.

Considering the positive TA dynamics at 1.60 eV, it is reasonable to assume $\sigma_D < \sigma_1 < \sigma_m$, implying $A_2 > 0$ and $B_2 > 0$. Therefore, the relationship in Eq. 3 describes a second-order polynomial dependence of the slow TA process on the pump fluence. This can be verified through fitting the measurement data by the blue-filled circles in the inset of Fig. 4C. Thus, our experimental results and the analyses summarized in Fig. 4 definitively determine model ④ in Fig. 1C as the dominant configuration for $WO_{2.72}$ and define the fingerprint features of oxygen vacancies located at two fixed lattice sites in the crystal structure of $WO_{2.72}$.

On this basis, we can resolve the electronic bandstructures of $WO_{2.72}$ and align them with the TA spectroscopic response, as shown in Fig. 4D. Figure 4D shows the TDOS distribution (open circles) and the fitting (solid red curve) by multiple Gaussian functions with different peak positions. The electronic bandstructures of $WO_{2.72}$ can thus be decomposed into multiple bands numbered I to VI. For comparison, the TDOS for $WO_{2.9}$ is also included in Fig. 4D by the green-filled circles. The corresponding energy levels with possible electronic transitions are summarized in Fig. 4E. For simplicity, the 2PA of the probe pulse is not included in Fig. 4E.

For the ground-state bands of $WO_{2.72}$ in Fig. 4E, we observe that band I, centered at $E_D = -0.8$ eV, becomes dominant, as indicated by the blue highlight in Fig. 4D, instead of band II that includes the Fermi level. Excitations through 1PE (❶) and 2PE (❷) processes, corresponding to transitions from E_D to populate E_0 and E_m, respectively, become non-negligible, in addition to ❸ and ❹. This enhances ground-state absorption at E_0 (❻) and exciton absorption at E_m (❼). This also explains why the amplitude of the TA dynamics for $WO_{2.72}$ is much larger than that for $WO_{2.9}$. Meanwhile, bleaching of the ground-state absorption in ❺ becomes much stronger than that in ❻, because the TDOS in band I is larger than that in band II, explaining the greatly broadened positive TA spectra for $WO_{2.72}$. Moreover, negative TA spectra are observed at photon energies larger than 1.8 eV, which agrees with the energy difference between bands I and III, as indicated by the dashed double arrow in Fig. 4E. Thus, the positive TA covers a broad band extending from 1.4 to more than 1.8 eV, which is consistent with the observations in Fig. 4A and fig. S7.

Figure 4D also reveals that the higher-lying bandgap around 2.5 eV in $WO_{2.9}$ becomes smeared in $WO_{2.72}$, where band V fills the space between IV and VI, as indicated by the yellow highlight. This explains the absence of the metastable state E_n in $WO_{2.72}$. A two-stage TA process is clearly observed for $WO_{2.72}$ when pumped at either 1.55 or 3.1 eV, whereas a definite three-stage process is observed for $WO_{2.9}$, as shown in Fig. 4B. This also explains the missing negative feature for a delay <400 fs centered at 1.61 eV in Fig. 4A as compared with Fig. 2A.

Although the bandgap centered at 0.5 eV between bands II and III is still present in $WO_{2.72}$, considerable overlapping exists between them, as indicated by the red highlight. This change causes a strong and fast back transfer from E_m to E_0 and consequently a much shorter lifetime of E_m excitons in $WO_{2.72}$ than that in $WO_{2.9}$, as clearly seen in the inset of Fig. 4B and fig. S8. Furthermore, the enhanced population on E_0 due to the pumping transition from E_D to E_0 compensates for much of the bleaching of E_0 absorption, thereby explaining the blue shift of the negative TA in Fig. 4A and fig. S7.

In Fig. 4F, we plot the TA spectrum at a delay of 2.5 ps for pumping at 1.55 eV. Two-photon processes were not involved in this stage. The negative TA observed for ❺ and ❻ is clearly due to bleaching of the ground-state absorption. The two distinctly separated bands indicated by the blue and green highlights verify the structures of bands I and II, respectively. The positive TA in Fig. 4F can be primarily attributed to exciton absorption at E_m (❼).

Preference rule in the formation of oxygen vacancies

The above determined oxygen-vacancy configuration in Fig. 2C-④ implies that the two oxygen vacancies tend to be located as close as

possible, as compared with the other three configurations. However, this violates the lowest formation energy rule for the whole system of the crystal structures, as revealed by the calculation results in table S1. Therefore, local structural mechanisms need to be analyzed to understand the observed preference. Figure 5 shows a local view of all W—O bonds surrounding a W atom for WO_3, $WO_{2.9}$, and $WO_{2.72}$, respectively, which are labeled by B1 to B6.

The oxygen atoms replaced by vacancies are highlighted by solid red circles. The second oxygen atom to be lost is highlighted by a red dashed circle in the lattice structures of WO_3 and $WO_{2.9}$, which is bonded to W by B5. The calculated bond length and bond population values are listed in table S2, where the value of bond population actually reflects the corresponding bonding energy. For WO_3, bonds B5 and B6 have the lowest bond population values, which agrees perfectly with the locations of the oxygen vacancies in $WO_{2.72}$. This also suggests that even for $WO_{2.9}$, the single oxygen vacancy tends to be located at one of the dash-circled lattice sites in the left panel of Fig. 5. Such a preference completely agrees with the observed ordered defect structure with a regular stair-step shape in the high-angle annular dark field–scanning transmission electron microscopy studies (*13*). The preferred configuration does not contradict the fact that the location of the oxygen vacancy has little influence on the TDOS distribution, as shown in fig. S2. After losing one oxygen atom in the unit cell of WO_3, the bond length and bond population are only slightly modified for B1 to B4 in $WO_{2.9}$, where B1 (+23.9%) and B4 (+8.8%) become shorter and stronger (highlighted by solid dashes in yellow), whereas B2 (−25.6%) and B3 (−15.6%) become longer and weaker (highlighted by dotted dashes). However, the bond parameters remain constant for B5, which imply lowest bonding energy and favor losing of the oxygen atom bonded to W by B5 during the formation of $WO_{2.72}$. After the breaking of bond B5 for losing a second oxygen atom, bonds B1 (−9.6%) and B4 (−17.2%) become weaker, whereas B2 (+3.4%) and B3 (+76.3%) become stronger. Compared with slight modifications on bonds B1, B2, and B4, a large enhancement of B3 would be induced by losing a second oxygen atom indicated by a thick yellow dash in the mid panel of Fig. 5, implying a more stable system for the transition from $WO_{2.9}$ to $WO_{2.72}$ through breaking B5. This explains consistently the oxygen-vacancy configuration of $WO_{2.72}$, as shown by the right panel of Fig. 5. Thus, we discovered a perfect agreement between the TA spectroscopy–determined and the chemical bond–suggested oxygen-vacancy configuration. Considering that debonding occurs first in the stepwise reduction reactions, the formation of oxygen vacancies on the weakest bonds agrees with the basic chemical rules. More specifically, our detailed analysis of the crystal structure of $WO_{2.72}$ found that the two oxygen vacancies are, in fact, ortho-positioned to a single W atom, which is different from all other O—W bonds. These consistencies solidly confirm the experimental observations in this work using femtosecond spectroscopy, implying an attainment of true visualization of the oxygen vacancies in both $WO_{2.9}$ and $WO_{2.72}$.

On the basis of the above experimental investigations and physical analysis, we present a more general picture in fig. S9 to summarize our investigation routes for better understanding the logic relationships between different sections. We summarize the following outlook aspects to highlight the importance, advantages, and potential applications of this presented strategy:

1) Femtosecond TA spectroscopy provides a powerful tool for studying this class of problem. It gives information on the lifetime of different dynamics for determining different excited states, the transient spectral features for distinguishing different energy bands, the multiphoton processes for revolving precisely the energy-level locations, and the multistage evolution for tracing precisely the electronic transition routes. In particular, all of these performances have a femtosecond time resolution; therefore, they ensure high accuracy of the experimental data.

2) Modeling using first-principle calculations involves no approximations and artificial modification depending on different structures or materials. This ensures the objectiveness and accuracy of the calculation results. Although the change in the oxygen content in the studied tungsten oxides is small, the calculated bandstructures show clearly discriminable differences between different oxides with different oxygen vacancy configurations. The difference can be observed clearly in the shape and amplitude of the TDOS spectrum both for the defect band and for the valance and conduction bands, as verified by Figs. 2, D and E, 3D, and 4D. All the above discussions evidence the reliability and accuracy of the fsV strategy through combining femtosecond spectroscopy and TDOS calculations.

3) The fsV method combining ultrafast optical spectroscopy and bandstructure calculation can be directly extended to oxides of other metals, which is based on substitution of crystal structures and consideration of proper oxygen concentrations. First-principle calculation is an effective access to obtain the bandstructure distribution of

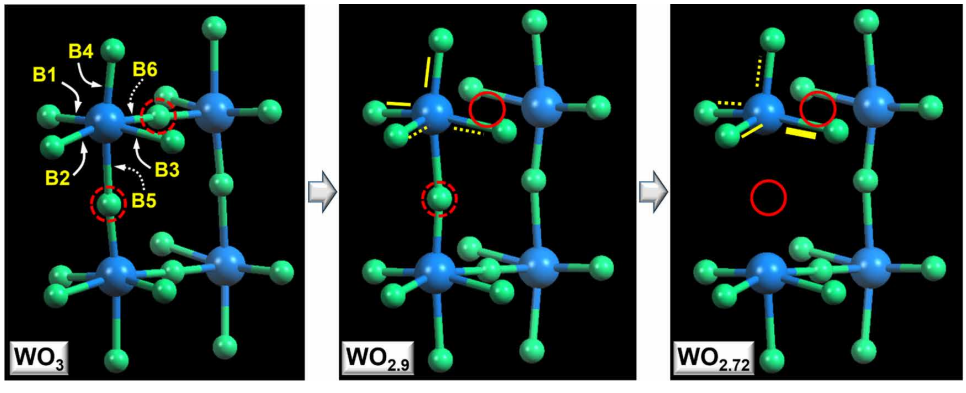

Fig. 5. Chemical bond configurations for WO_3, $WO_{2.9}$, and $WO_{2.72}$ with different oxygen-vacancy distributions. Dashed arrows indicate weakest bonds (B5 and B6), according to the theoretical calculations.

crystalline materials. In combination with ultrafast optical spectroscopy, it becomes possible to disclose the structural nature with high specificity of the metal oxide materials. Furthermore, such structure- or composition-based specificity is not only limited to oxygen vacancy defects. Thus, the fsV strategy can be applied to the design of new materials and supplies guidance for the practical preparation processes. Furthermore, this strategy can be used to predict the structural stability and hence their reactivity, as well as the resultant variety of products.

4) The combination of ultrafast optical spectroscopy and first-principle modeling enables fingerprint identification of specific oxygen-vacancy configurations in metal oxides. This potentially enables the integration of the presented method with the intelligent algorithms, such as machine learning approaches, to deal with high-throughput identification of oxygen vacancy configurations, as well as prediction of compositions, for a large variety of metal oxides. This may open a path to high-efficiency screening of structures or compositions in new material design.

CONCLUSIONS

We are able to "visualize" the oxygen-vacancy configurations in metal oxides using "photons" in femtosecond time scale, breaking through the limits set by the available microscopic techniques using "electrons or x-rays." The revealed physics verifies the existence of preference mechanisms for the removal of oxygen atoms from the lattices in the reduction of metal oxides. This generalizes an optoelectronic approach for atom-scale determination of the spatial arrangements of oxygen deficiencies in metal oxides using femtosecond spectroscopy. Using tungsten oxides as examples, we located the oxygen deficiency in $WO_{2.9}$ with respect to WO_3 and the oxygen vacancies in $WO_{2.72}$ from multiple possibilities by aligning the TDOS distribution with the measured photoelectronic transitions. Our findings of the preferred lattice sites of the oxygen vacancies not only revealed new photoelectronics but also suggest crystal structure determination with high precision and reliability practically applicable to a variety of metal oxides. This is important to both optoelectronics and materials science. In particular, the precise determination and control of oxygen-vacancy configuration will definitely push forward the development of chemiresistive sensors based on the reduction/oxidization interactions of metal oxides with the detected substance.

MATERIALS AND METHODS

Sample preparation

We prepared bulk samples of tungsten oxides, WO_3, $WO_{2.9}$, and $WO_{2.72}$, by sintering powders with a mean particle size of ~1 μm in a furnace filled with highly purified argon gas. We then polished the surfaces of the fully densified bulk samples to obtain sufficiently high reflectivity of the incident light beams.

TA measurements

We carried out the TA spectroscopic measurements using a femtosecond pump-probe system, where the Ti:sapphire amplifier (Legend Elite Series from Coherent Inc.) supplied 1-kHz pump pulses at 800 nm (1.55 eV) with a pulse length of about 150 fs. The direct output of the amplifier was frequency-doubled using a β-barium borate crystal to produce pump pulses at 400 nm (3.1 eV). A small portion of the 800-nm pulses was focused into 1-mm-thick heavy water in a cuvette to produce supercontinuum, which extends from about 1.1 to 3.6 eV (from about 1120 to 340 nm), and was used as the probe.

First-principle calculation

We modeled the local atomic configurations of $WO_{2.9}$ and $WO_{2.72}$ by removing oxygen atoms from the unit cell of WO_3; i.e., we introduced oxygen vacancies into the crystal structure of WO_3 (*19*, *20*). We performed calculations with the Cambridge Serial Total Energy Package (*38*) using density functional theory with the hybrid functional PBE0 (*39*). For electron-ion interactions, we used the $5d^4 6s^2$ and $2s^2 2p^4$ pseudopotential valence states for W and O, respectively. We set the cutoff energy of the atomic wave functions to be 600 eV. For electronic relaxation, we iterated the system energy until a tolerance of 10^{-6} eV per atom was attained.

SUPPLEMENTARY MATERIALS

Supplementary material for this article is available at http://advances.sciencemag.org/cgi/content/full/6/10/eaax9427/DC1

Fig. S1. Comparison between the Gibbs free energies of WO_3, $WO_{2.9}$, and $WO_{2.72}$ in a temperature range of 300 to 900 K.

Fig. S2. The possible crystal structures and the corresponding TDOS distributions of $WO_{2.9}$.

Fig. S3. TA measurements on WO_3 with pump photon energies of 3.1 and 1.55 eV and the corresponding alignments with the calculated TDOS distributions.

Fig. S4. TA spectra at different time delays for measurements on $WO_{2.9}$.

Fig. S5. TA dynamics measured on $WO_{2.9}$ at 1.51 and 1.6 eV for pumping at 3.1 eV.

Fig. S6. Pump fluence dependence of the TA dynamics measured on $WO_{2.9}$ using a pump at 1.55 eV.

Fig. S7. Comparison between the TA spectra of $WO_{2.72}$ (at a delay of 0.4 ps) and $WO_{2.9}$ (at delays of 0.25 and 0.4 ps).

Fig. S8. TA dynamics measured for $WO_{2.72}$ at 1.50 and 1.61 eV and $WO_{2.9}$ at 1.50 eV.

Fig. S9. Diagrammatic summary of the logic relationships between different sections.

Table S1. The calculated formation energies of $WO_{2.72}$ corresponding to the four kinds of configurations with different distributions of oxygen vacancies.

Table S2. Bond length and bond population for chemical bonds of WO_3, $WO_{2.9}$, and $WO_{2.72}$.

REFERENCES AND NOTES

1. R. F. Cava, W. F. Peck Jr., J. J. Krajewski, Enhancement of the dielectric constant of Ta_2O_5 through substitution with TiO_2. *Nature* **377**, 215–217 (1995).
2. M. Venkatesan, C. B. Fitzgerald, J. M. D. Coey, Thin films: Unexpected magnetism in a dielectric oxide. *Nature* **430**, 630 (2004).
3. I. Ferain, C. A. Colinge, J.-P. Colinge, Multigate transistors as the future of classical metal-oxide-semiconductor field-effect transistors. *Nature* **479**, 310–316 (2011).
4. Z. Wang, P. K. Nayak, J. A. Caraveo-Frescas, H. N. Alshareef, Recent developments in p-type oxide semiconductor materials and devices. *Adv. Mater.* **28**, 3831–3892 (2016).
5. R. A. Mckee, F. J. Walker, M. F. Chisholm, Physical structure and inversion charge at a semiconductor interface with a crystalline oxide. *Science* **293**, 468–471 (2001).
6. Y. Zhao, X. Li, B. Yan, D. Xiong, D. Li, S. Lawes, X. Sun, Recent developments and understanding of novel mixed transition-metal oxides as anodes in lithium ion batteries. *Adv. Energy Mater.* **6**, 1502175 (2016).
7. J. Rousset, E. Saucedo, D. Lincot, Extrinsic doping of electrodeposited zinc oxide films by chlorine for transparent conductive oxide applications. *Chem. Mater.* **21**, 534–540 (2009).
8. Y. H. Li, P. F. Liu, L. F. Pan, H. F. Wang, Z. Z. Yang, L. R. Zheng, P. Hu, H. J. Zhao, L. Gu, H. G. Yang, Local atomic structure modulations activate metal oxide as electrocatalyst for hydrogen evolution in acidic water. *Nat. Commun.* **6**, 8064 (2015).
9. K. Manthiram, A. P. Alivisatos, Tunable localized surface plasmon resonances in tungsten oxide nanocrystals. *J. Am. Chem. Soc.* **134**, 3995–3998 (2012).
10. A. Zaffora, F. D. Quarto, C. Kura, Y. Sato, Y. Aoki, H. Habazaki, M. Santamaria, Electrochemical oxidation of Hf–Nb alloys as a valuable route to prepare mixed oxides of tailored dielectric properties. *Adv. Electron. Mater.* **4**, 1800006 (2018).
11. Z. F. Huang, J. Song, L. Pan, X. Zhang, L. Wang, J.-J. Zou, Tungsten oxides for photocatalysis, electrochemistry, and phototherapy. *Adv. Mater.* **27**, 5309–5327 (2015).
12. K.-U. Demasius, T. Phung, W. Zhang, B. P. Hughes, S.-H. Yang, A. Kellock, W. Han, A. Pushp, S. S. P. Parkin, Enhanced spin–orbit torques by oxygen incorporation in tungsten films. *Nat. Commun.* **7**, 10644 (2016).

13. B. Ingham, S. C. Hendy, S. V. Chong, J. L. Tallon, Density-functional studies of tungsten trioxide, tungsten bronzes, and related systems. *Phys. Rev. B* **72**, 075109 (2005).
14. F. Wang, C. Di Valentin, G. Pacchioni, Semiconductor-to-metal transition in WO_{3-x}: Nature of the oxygen vacancy. *Phys. Rev. B* **84**, 073103 (2011).
15. S. Han, X. Yang, Y. Zhu, C. Tan, X. Zhang, J. Chen, Y. Huang, B. Chen, Z. Luo, Q. Ma, M. Sindoro, H. Zhang, X. Qi, H. Li, X. Huang, W. Huang, X. Sun, Y. Han, H. Zhang, Synthesis of WO_n-WX_2 (n= 2.7, 2.9; X=S, Se) heterostructures for highly efficient green quantum dot light emitting diodes. *Angew. Chem. Int. Edit.* **129**, 10622–10626 (2017).
16. J. Liu, Z. Zhang, Y. Zhao, X. Sun, S. Liu, E. Wang, Tuning the field-emission properties of tungsten oxide nanorods. *Small* **1**, 310–313 (2005).
17. H. Zheng, J. Z. Ou, M. S. Strano, R. B. Kaner, A. Mitchell, K. Kalantar-zadeh, Nanostructured tungsten oxide–properties, synthesis, and applications. *Adv. Funct. Mater.* **21**, 2175–2196 (2011).
18. M. Epifani, N. Garcia-Castello, J. D. Prades, A. Cirera, T. Andreu, J. Arbiol, P. Siciliano, J. R. Morante, Suppression of the NO_2 interference by chromium addition in WO_3-basedammonia sensors. Investigation of the structural properties and of the related sensing pathways. *Sens. Actuators B* **187**, 308–312 (2013).
19. J. Yeom, U. S. Santos, M. Chekini, M. Cha, A. F. de Moura, N. A. Kotov, Chiromagnetic nanoparticles and gels. *Science* **359**, 309–314 (2018).
20. J. E. Katz, X. Y. Zhang, K. Attenkofer, K. W. Chapman, C. Frandsen, P. Zarzycki, K. M. Rosso, R. W. Falcone, G. A. Waychunas, B. Gilbert, Electron small polarons and their mobility in iron (Oxyhydr) oxide nanoparticles. *Science* **337**, 1200–1203 (2012).
21. L. M. Carneiro, S. K. Cushing, C. Liu, Y. D. Su, P. D. Yang, A. P. Alivisatos, S. R. Leone, Excitation-wavelength-dependent small polaron trapping of photoexcited carriers in α-Fe_2O_3. *Nat. Mater.* **16**, 819–825 (2017).
22. X. P. Zhang, C. Y. Huang, M. Wang, P. Huang, X. K. He, Z. Y. Wei, Transient localized surface plasmon induced by femtosecond interband excitation in gold nanoparticles. *Sci. Rep.* **8**, 10499 (2018).
23. Y. H. Lin, X. P. Zhang, Ultrafast multipolar plasmon for unidirectional optical switching in a hemisphere-nanoshell array. *Adv. Opt. Mater.* **5**, 1661088 (2017).
24. W. D. Xu, J. A. McLeod, Y. G. Yang, Y. M. Wang, Z. W. Wu, S. Bai, Z. C. Yuan, T. Song, Y. S. Wang, J. J. Si, R. B. Wang, X. Y. Gao, X. P. Zhang, L. J. Liu, B. Q. Sun, Iodomethane-mediated organometal halide perovskite with record photoluminescence lifetime. *ACS Appl. Mater. Interfaces* **8**, 23181–23189 (2016).
25. I. A. Howard, J. M. Hodgkiss, X. P. Zhang, K. R. Kirov, H. A. Bronstein, C. K. Williams, R. H. Friend, S. Westenhoff, N. C. Greenham, Charge recombination and exciton annihilation reactions in conjugated polymer blends. *J. Am. Chem. Soc.* **132**, 328–335 (2010).
26. T. P. Ma, Y. Yang, Z. Ding, Z. H. Chen, H. B. Zhao, P. Werner, S. P. P. Parkin, Y. Z. Wu, Manipulating charge ordering in Fe_3O_4 by field cooling. *Phys. Rev. B* **95**, 014103 (2017).
27. L. Le Guyader, M. Savoini, S. El Moussaoui, M. Buzzi, A. Tsukamoto, A. Itoh, A. Kirilyuk, T. Rasing, A. V. Kimel, F. Nolting, Nanoscale sub-100 picosecond all-optical magnetization switching in GdFeCo Microstructures. *Nat. Commun.* **6**, 5839 (2015).
28. J. Becker, A. Tsukamoto, A. Kirilyuk, J. C. Maan, T. Rasing, P. C. M. Christianen, A. V. Kimel, Ultrafast magnetism of a ferrimagnet across the spin-flop transition in high magnetic fields. *Phys. Rev. Lett.* **118**, 117203 (2017).
29. X. Ma, F. Fang, Q. Li, J. Zhu, Y. Yang, Y. Z. Wu, H. B. Zhao, G. Lüpke, Ultrafast spin exchange-coupling torque via photo-excited charge-transfer processes. *Nat. Commun.* **6**, 8800 (2015).
30. L. Wibmer, S. Lages, T. Unruh, D. M. Guldi, Excitons and trions in one-photon- and two-photon-excited MoS_2: A study in dispersions. *Adv. Mater.* **30**, 1706702 (2018).
31. D. A. Fishman, C. M. Cirloganu, S. Webster, L. A. Padilha, M. Monroe, D. J. Hagan, E. W. Van Stryland, Sensitive mid-infrared detection in wide-bandgap semiconductors using extreme non-degenerate two-photon absorption. *Nat. Photon.* **5**, 561–565 (2011).
32. A. T. Dinsdale, SGTE data for pure elements. *CAL* **15**, 317–425 (1991).
33. F. Wang, C. Di Valentin, G. Pacchioni, Electronic and structural properties of WO_3: A systematic hybrid DFT study. *J. Phys. Chem. C* **115**, 8345–8353 (2011).
34. M. N. Huda, Y. Yan, C.-Y. Moon, S.-H. Wei, M. M. Al-Jassim, Density-functional theory study of the effects of atomic impurity on the band edges of monoclinic-WO_3. *Phys. Rev. B* **77**, 195102 (2008).
35. X. P. Zhang, Y. J. Xia, R. H. Friend, C. Silva, Sequential absorption processes in two-photon-excitation transient absorption spectroscopy in a semiconductor polymer. *Phys. Rev. B* **73**, 245201 (2006).
36. X. P. Zhang, Y. Xia, R. H. Friend, Multiphoton excited photoconductivity in polyfluorene. *Phys. Rev. B* **75**, 245128 (2007).
37. J. Y. Bigot, V. Halte, J. C. Merle, A. Daunois, Electron dynamics in metallic nanoparticles. *Chem. Phys.* **251**, 181–203 (2000).
38. K. Parlinski, Z. Q. Li, Y. Kawazoe, First-principles determination of the soft mode in Cubic ZrO_2. *Phys. Rev. Lett.* **78**, 4063–4066 (1997).
39. J. P. Perdew, K. Burke, M. Ernzerhof, Generalized gradient approximation made simple. *Phys. Rev. Lett.* **77**, 3865–3868 (1996).

Acknowledgments

Funding: We acknowledge the support by National Natural Science Foundation of China (61735002, 51631002, 51425101, 51621003, 11574015, and 11434016) and the National Key Program of Research and Development (2018YFB0703902). **Author contributions:** X.Z. and X.S. designed this research and wrote this paper together. X.Z. did the data processing and analysis. R.H.F. advised physical investigations, data analysis, and improvements of the manuscript. F.T. did the first-principle calculations. X.S. and F.T. investigated on the models of the crystal structures. M.W. carried out the TA spectroscopic measurements. W.Z., H.H., and Y.L. prepared samples of tungsten oxides. **Competing interests:** The authors declare that they have no competing interests. **Data and materials availability:** All data needed to evaluate the conclusions in the paper are present in the paper and/or the Supplementary Materials. Additional data related to this paper may be requested from the authors.

Submitted 7 May 2019
Accepted 12 December 2019
Published 6 March 2020
10.1126/sciadv.aax9427

Citation: X. Zhang, F. Tang, M. Wang, W. Zhan, H. Hu, Y. Li, R. H. Friend, X. Song, Femtosecond visualization of oxygen vacancies in metal oxides. *Sci. Adv.* **6**, eaax9427 (2020).